Aperture Neuro

Sairanen V. Voxel-wise function-structure coupling with diffusion-weighted and functional MRI. *Aperture Neuro*. 2026;6. doi:10.52294/001c.172225

Original Research Articles

Voxel-wise function-structure coupling with diffusion-weighted and functional MRI

Viljami Sairanen, PhD[1,2] [a]

[1] Baby Brain Activity Center, Helsinki University Hospital and University of Helsinki, Helsinki, Finland, [2] Department of Radiology, Hämeenlinna Central Hospital, Hämeenlinna, Finland

Keywords: function-structure coupling, diffusion-weighted MRI, functional MRI, resting-state, fibre orientation distributions, graph Laplacian

https://doi.org/10.52294/001c.172225

Aperture Neuro

Vol. 6, 2026

Function-structure coupling methods often compare functional connectivity with regional structural connectomes derived from diffusion MRI tractography. Such regional representation can obscure spatially extended, indirect, or crossing-fibre structural support between functionally connected regions. This work proposes a voxel-wise function-structure coupling using a constrained-Laplacian framework that imposes observed fMRI-derived functional connectivity values on voxel-wise structural graphs derived from fibre orientation distributions (FODs) of individual subjects. The method produces graph potentials, voxel-edge current fields, and voxel-wise support maps that describe how functional relationships are accommodated by local diffusion-derived structural architecture. Evaluation consists of an in-silico diffusion phantom, inspection of local graph construction in coherent and crossing-fibre regions, seven resting-state fMRI network demonstrations in three Human Connectome Project subjects, test-retest analyses of the subjects, and a network parcellation scale analysis. A permutation analysis was used to investigate how much of each network can be explained by a common white matter structure and variation from this common backbone. Across subjects, median observed-null resemblance ranged from 0.578 to 0.630 for whole-map Pearson correlation and from 0.287 to 0.328 for top-5% Dice overlap. These findings support a conservative interpretation of voxel-wise FSC providing a spatially resolved quantitative representation of functional constraints on a diffusion-derived graph. Yet, the present experiments do not establish anatomical network specificity.

1. INTRODUCTION

This work addresses a central question in neuroimaging: how are functional interactions between brain regions supported by the structural architecture of the brain? Functional interactions can be studied with functional MRI (fMRI),[1-3] whereas diffusion-weighted MRI (dMRI) provides sensitivity to tissue microstructure and white-matter organization.[4-6] However, the common practice of representing the brain as a parcellation-level graph imposes an inherent limitation: structural connectivity is reduced to connections between predefined regions, even though the underlying anatomy is continuous, spatially extended, and locally organized at a much finer scale. This work proposes a way to use the voxel-level structural information in investigation of the functional connections.

The structural connectome is often estimated using dMRI tractography, but streamline reconstructions are sensitive to modelling assumptions and may contain substantial false-positive and false-negative pathways.[7-10] This is particularly problematic for parcellation-level function-structure analyses: a functional relationship between two regions is not necessarily supported by a single direct reconstructed tract between the same parcels. Instead, functional connectivity may reflect indirect, polysynaptic, distributed, or spatially extended structural support.[11-16] Together, these issues motivate complementary uses of dMRI in which the diffusion-derived brain microstructure is modelled more directly, rather than first reduced to a parcel-wise tractography connectome.

[a] **Corresponding Author:**
Viljami Sairanen, PhD (viljami.sairanen@helsinki.fi)
Baby Brain Activity Center, Children's Hospital, Helsinki University Hospital and University of Helsinki
Department of Radiology, Hämeenlinna Central Hospital
Helsinki, Finland

A relevant lineage of dMRI methods is graph-based modelling. Early graph-theoretical tractography represented the brain as a voxel-wise graph, with voxels as nodes and local diffusion information defining edge weights between neighbouring voxels.[17,18] Related fast-marching, geodesic, and global tractography frameworks similarly used diffusion information to define local costs, transition probabilities, or optimization problems over the image domain.[19-23] While these methods were mainly designed to recover anatomical pathways, they were based on a more universal idea: dMRI can define a voxel-wise structural graph. Their limited subsequent use likely reflects the dominance of streamline tractography and parcel-wise connectomics as more practical and interpretable summaries of dMRI data, rather than a failure of the voxel-wise graph idea itself.

The present work reopens this voxel-wise diffusion-graph view with a new purpose. Rather than searching the graph for the most likely or shortest dMRI pathways, I propose to use it as a structural network on which resting-state fMRI-derived functional coupling values are imposed as boundary conditions. This allows structural support to be modelled before it is compressed into parcel-wise edges, reducing the problem of indirect structural links between large brain parcels.

The proposed method should not be seen as another path-reconstruction algorithm as the computational objective is to solve a constrained field over the graph rather than to reconstruct a streamline trajectory. This distinction applies to the solving step, not to the reliability of the graph itself. The structural graph remains diffusion-derived and inherits uncertainty from fibre orientation distribution (FOD) estimation, partial-volume effects, crossing-fibre ambiguity, limited spatial and angular resolution, registration, and the absence of explicit anatomical boundary constraints.[7] Tractogram-like displays derived from the solved current field are therefore secondary visualizations rather than the primary output.

This study builds on my previous constrained-Laplacian formulation of brain function-structure coupling.[24] In that work, functional relationships were imposed as constraints on a structural graph obtained from dMRI tractography, producing edge-centric estimates of how functional coupling is supported by structural connectivity. The present method extends this idea from regional structural connectomes to voxel-level. Instead of starting from a parcel-wise structural connectivity matrix, the whole-brain graph is constructed from FODs and uses the functional coupling to condition the resulting structural field. A Python implementation of the proposed method is available at https://github.com/vilsaira/fscpy.

2. THEORY

The voxel-wise function-structure coupling (FSC) formulation follows the constrained-Laplacian FSC terminology introduced previously,[24] but replaces the regional structural connectome with voxel-wise dMRI-derived structures. The structural network is represented as an undirected weighted graph

$$G = (V, E, W), \tag{1}$$

where V is the set of voxels (nodes), E is the set of neighbouring voxel interfaces (edges), and W is the weighted adjacency matrix. This voxel-wise graph representation follows earlier dMRI graph formulations in which voxels are treated as graph nodes and local diffusion information defines edge weights between neighbouring voxels.[17,18,25-27]

To create this graph representation, fibre orientation distributions (FODs) derived using constrained spherical deconvolution[9,28] are used. In contrast to graph-based tractography, the FOD-derived weighted adjacency matrix W defines the structural conductances on which the constrained FSC problem is solved instead of finding purely structural routes.

Mathematically, FOD can be defined as $F_i(\mathbf{u})$ in voxel i evaluated in direction $\mathbf{u}$. Because spherical harmonic FODs may contain small negative values, only the positive component is used:

$$F_i^+(\mathbf{u}) = \max\left(F_i(\mathbf{u}), 0\right). \tag{2}$$

To suppress non-directional FOD amplitude, an orientation-selective support function $s_i(\mathbf{u})$ is defined by subtracting the local isotropic component,

$$\begin{aligned} s_i(\mathbf{u}) &= \max\left(F_i^+(\mathbf{u}) - \alpha \bar{F}_i,\ 0\right), \\ \bar{F}_i &= \frac{1}{4\pi}\int_{\mathbb{S}^2} F_i^+(\mathbf{v})\, d\mathbf{v}, \end{aligned} \tag{3}$$

where α controls the suppression of isotropic support. The default choice $\alpha = 1$ retains directional FOD amplitude above the local isotropic baseline.

For neighbouring voxels i and j, $\mathbf{u}_{ij}$ is the unit direction between voxels, and ℓ_{ij} is the corresponding physical edge length. The voxel-interface weight w_{ij} can then be defined as bidirectional endpoint support,

$$w_{ij} = \frac{1}{\ell_{ij}}\sqrt{s_i(\mathbf{u}_{ij}) s_j(-\mathbf{u}_{ij})}. \tag{4}$$

This formulation ensures that an interface w_{ij} receives high conductance only when both adjacent voxels provide oriented support for the interface direction. The geometric mean acts as a bottleneck rule: high support at one endpoint cannot compensate for absent support at the other. Simple toy examples to illustrate this are shown in Figure 1.

Although voxel-wise FODs are usually antipodally symmetric, the bidirectional evaluations on voxel interfaces are conceptually distinct because the edge represents a region between two neighbouring orientation fields. This neighbourhood-aware view is related to the broader observation that adjacent voxels contain information about local fibre geometry that is not fully captured by purely voxel-wise symmetric representations.[29] The present method does not require asymmetric FODs, but it uses both sides of the voxel interface when assigning structural support.

The weighted adjacency matrix is defined by $W_{ij} = w_{ij}$ for $(i,j) \in E$ and $W_{ij} = 0$ otherwise. The graph is undirected, so $W = W^\top$ and the formulation does not infer directed or source-to-target influences. The degree matrix and graph Laplacian are

$$D = \operatorname{diag}\left(\sum_j W_{ij}\right), \qquad \mathcal{L} = D - W. \tag{5}$$

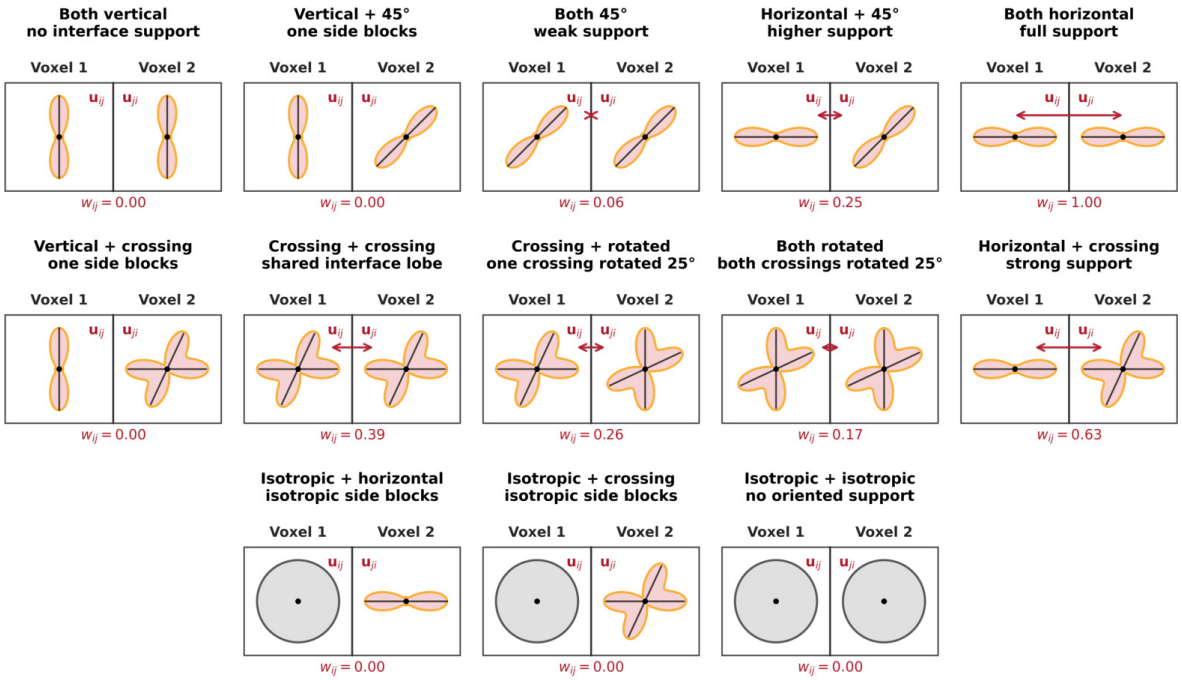

Figure 1. Illustration of bidirectional FOD support on two-voxel interfaces. Edge support is strongest when both adjacent FODs are aligned with the interface direction and disappears when either endpoint lacks directional support. Crossing-fibre examples show that an interface can be supported by the lobe aligned with the interface, whereas isotropic examples show that isotropic FOD amplitude alone does not create directional conductance.

Equivalently, using the edge-incidence representation,[24]

$$\mathcal{L} = B_G C_G B_G^\top, \tag{6}$$

where B_G is the oriented incidence matrix of the voxel graph and $C_G = \mathrm{diag}(w_{ij})$ contains the voxel-edge conductances. This follows standard spectral graph theory and graph signal processing notation.[30,31] The subscript G distinguishes the voxel-graph incidence matrix from the functional-constraint incidence matrix defined next.

To impose functional coupling (FC) values as potential difference constraints, define $s_{\mathrm{fc}} \in \mathbb{R}^n$ which contains the n imposed coupling values, and $B_{\mathrm{fc}} \in \mathbb{R}^{|V|\times n}$ which is the functional-constraint incidence matrix whose columns define the constrained node pairs. The empirical constraints are

$$B_{\mathrm{fc}}^\top \phi = s_{\mathrm{fc}}, \tag{7}$$

where $\phi \in \mathbb{R}^{|V|}$ contains the voxel-wise graph potentials. Using modified nodal analysis,[24,32,33] these constraints are solved jointly with the voxel-wise Laplacian system as

$$\begin{bmatrix} \mathcal{L} & B_{\mathrm{fc}} \\ B_{\mathrm{fc}}^\top & 0 \end{bmatrix} \begin{bmatrix} \phi \\ i_s \end{bmatrix} = \begin{bmatrix} 0 \\ s_{\mathrm{fc}} \end{bmatrix}, \tag{8}$$

where $i_s \in \mathbb{R}^n$ are auxiliary source currents enforcing the imposed functional constraints.

Once nodal potentials ϕ have been solved, voxel-edge flows or currents are obtained by applying the graph gradient and weighting it by the voxel-edge conductances:

$$f = C_G B_G^\top \phi. \tag{9}$$

For an individual voxel interface (i, j), this corresponds to

$$I_{ij} = w_{ij}\left(\phi_i - \phi_j\right). \tag{10}$$

The sign of I_{ij} depends on the arbitrary orientation assigned to the edge, whereas $|I_{ij}|$ indicates how strongly the imposed functional constraints use that local structural interface. A voxel-wise support J_i map is obtained by summing the magnitudes of all edge currents incident on each voxel,

$$J_i = \sum_{j \in \mathcal{N}(i)} |I_{ij}|, \tag{11}$$

where $\mathcal{N}(i) = \{j : (i, j) \in E\}$ is the set of graph neighbours of voxel i.

The resulting potentials, edge flows, and support maps retain the edge-centric constrained-Laplacian interpretation of the previous FSC model,[24] but the structural network is now a voxel-wise FOD-derived graph rather than a regional tractography-derived connectome. This also connects voxel-wise FSC to broader Laplacian and connectome-harmonic approaches in which structural graph operators constrain functional organization.[12,14,34,35] The implicit circuit analogy remains mathematical rather than biophysical: potentials and currents describe how the structural graph accommodates imposed statistical relationships, not causal neural signal transmission.

The interface conductances should be interpreted as FOD-derived model weights rather than measurements of anatomical connection strength, axonal density, or fibre cross-sectional area. Baseline subtraction and geometric-mean weighting require directional support at both sides of an interface, but do not establish that the interface represents a genuine anatomical fibre continuation. The current formulation contains no global conductance-calibra-

tion step equivalent to tractogram-weighting approaches such as SIFT2.[36]

3. METHODS

The evaluation consisted of six complementary stages. First, an in-silico FiberCup experiment was used as an implementation-level sanity check of graph construction, constraint encoding, and support extraction on a known synthetic structure (Section 3.1). Second, voxel-wise FSC was applied to HCP data using the Schaefer200 parcellation[37] to evaluate the method at a finer functional scale, generate seven-network support maps in all three subjects, and compare voxel-wise FSC with tractography-style displays (Sections 3.2 to 3.4). Third, random permutations of FC-pair labels were performed in all three subjects to measure how strongly support-map organization depended on the anatomical placement of the functional constraints (Section 3.5). Fourth, the analysis was repeated with the 68-region Desikan-Killiany parcellation[38] to match the original region-level FSC study[24] (Section 3.6). Fifth, Schaefer parcellations containing 100-1000 regions were evaluated to separate effects of parcel scale from differences between atlas construction schemes. Sixth, within-subject test-retest reproducibility was assessed using matched phase-encoding directions (Section 3.7). An overview of the voxel-wise FSC workflow is shown in Figure 2.

3.1. IN-SILICO FIBERCUP SANITY CHECK

The voxel-wise FSC implementation was evaluated using the FiberCup diffusion phantom, which provides a controlled synthetic structure with known fibre configurations.[39-41] The aim was not to establish biological validity, but to provide an implementation-level sanity check showing that imposed functional relationships could be mapped onto a known FOD-derived fibre architecture and that the problem would be numerically solvable.

The in-silico functional simulation followed the FiberCup experiment described in my previous work.[24] In that experiment, regional functional connectivity was generated from simulated node dynamics on a tractography-derived structural graph. Five functional relationships were retained as imposed constraints. Four of these corresponded to direct structural connections in the original graph, whereas the fifth was indirect meaning that the regions were not connected by a single tractography bundle but required one intermediate node.

In the present analysis, the same functional constraints were imposed on a voxel-wise graph constructed directly from the FiberCup FOD image. Voxels were treated as graph nodes, and neighbouring voxel conductances were derived from bidirectional FOD support across each voxel interface. The resulting current-magnitude maps and pairwise path summaries were inspected to test whether direct relationships followed the expected fibre bundles and whether the previously indirect relationship behaved consistently with the structural possibilities of the voxel-wise FOD network. Failure to produce plausible support patterns would indicate a problem in graph construction, constraint encoding, or path extraction.

3.2. HCP DATA AND VOXEL-WISE GRAPH CONSTRUCTION

Voxel-wise FSC was evaluated in three Human Connectome Project (HCP) subjects: 130013, 106824, and 419239.[42-44] For each subject, resting-state fMRI data were used to calculate functional connectivity (FC) matrices and dMRI data were used to estimate voxel-wise fibre orientation distributions. The acquisition and preprocessing followed the HCP pipelines described in the original analysis.[24]

Qualitative tractography comparison was done with MRtrix3 using multi-shell, multi-tissue constrained spherical deconvolution, the unsupervised response-function approach, and probabilistic second-order integration over FODs (iFOD2).[45,46] Anatomically constrained tractography was used for the human HCP data.[47] One million streamlines were generated with minimum and maximum lengths of 5 and 250 mm and a normalized white-matter FOD cutoff of 0.05. All other iFOD2 tracking parameters were left at the MRtrix3 defaults and no tractogram filtering or weighting[36,48] was applied. Structural connectivity was summarized by counting streamlines connecting each pair of cortical regions. The tractogram was retained only as a qualitative representational comparison and not as a current-best-practice quantitative benchmark.

For voxel-wise FSC, each FOD image was converted into a voxel-wise structural graph using the conductance definition described in the Theory section. Graph nodes were FOD-supported voxels, and graph edges represented neighbouring voxel interfaces weighted by bidirectional FOD support. Cortical parcels were represented as ROI supernodes connected to adjacent graph boundary voxels, allowing regional FC constraints to enter the voxel-wise structural graph through multiple parcel-graph interfaces rather than through a single regional edge. This ROI-to-voxel graph interface is illustrated in Figure 2.

For each HCP analysis, observed resting-state FC values were imposed on the subject- and voxel-wise FOD graph using the constrained formulation described in the Theory section. The primary voxel-wise outputs were the solved graph potentials, voxel-edge current fields, and derived voxel-wise support maps.

3.3. SCHAEFER200 ANALYSIS

The main HCP voxel-wise analysis used the 200-region Schaefer cortical parcellation.[37] This parcellation was used because it provides a finer functional scale than Desikan-Killiany and includes parcel labels that assign each region to one of the canonical Yeo intrinsic functional networks.[49] The Schaefer200 atlas was transformed to each subject's native HCP diffusion space using the HCP standard-to-native registration warp with nearest-neighbour interpolation, preserving integer labels. The warped atlas was used to define ROI supernodes and their interfaces with the voxel-wise FOD graph.

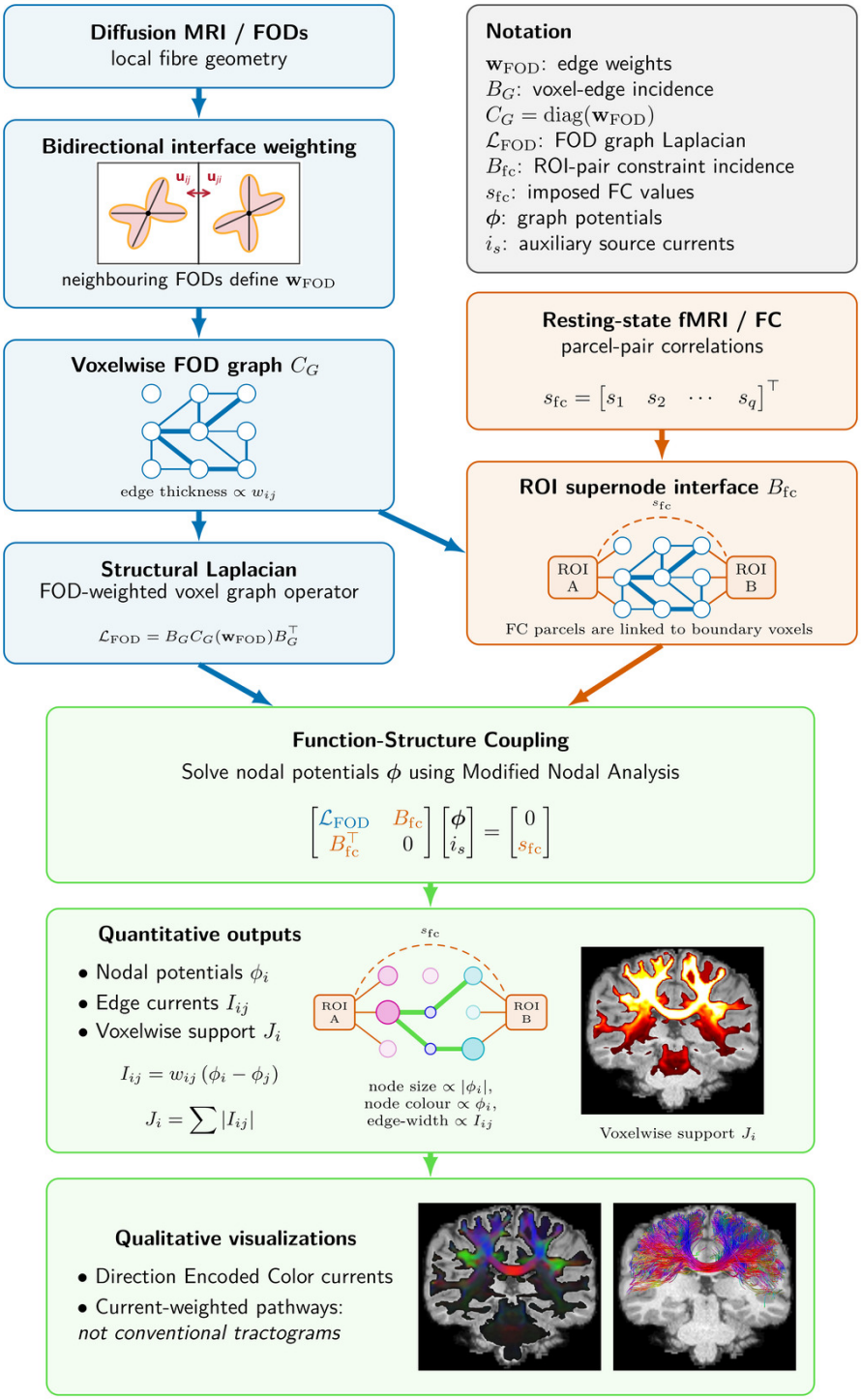

Figure 2. Overview of the voxel-wise FSC framework.

Schaefer200 functional connectivity matrices were computed from the four HCP resting-state runs corresponding to 1LR, 1RL, 2LR, and 2RL. Regional time series were extracted using the Schaefer200 atlas, Fisher transformed, scaled, and used as functional constraints in the voxel-wise FSC model. Voxel-wise FSC was then solved on the subject-wise FOD-derived graph using the graph construction and ROI-interface rules described above.

3.4. NETWORK VISUALIZATION

Using the Schaefer200 parcellation and Yeo's network assignments, network-level voxel-wise support maps were generated separately for the three subjects. Within each network, the 50 strongest finite positive Fisher-z FC values were selected. Pair selection was based solely on FC magnitude and was not constrained or balanced by hemisphere. The hemispheric distribution of the selected connections was therefore determined by the observed FC values rather than imposed by the analysis. The fixed count gave every

network the same number of pairwise contributions and it was a design choice for aggregation rather than a biological or statistical threshold. Each selected value was imposed on the subject-specific FOD graph, the resulting pairwise current magnitudes were accumulated within network, and voxel support was calculated as defined in the Theory section.

For the visualization, each complete three-dimensional network support map was L1-normalized by its total positive support to preserve comparisons of the relative spatial allocation of support while avoiding the full saturation produced by independently scaling every network.

The expected unrestricted null backbone was calculated from the mean unit-pair support over all 19900 unordered Schaefer200 parcel pairs and was L1-normalized in the same manner as the observed maps. Residual maps were obtained by subtracting this null reference from each L1-normalized observed network map. Positive and negative residuals therefore balance over the complete volume. The somatomotor network was additionally visualized as a voxel-wise FSC support map, a current-guided path-like summary of the same solved edge-current field, and a conventional tractogram selected using the same network masks. The path-like display was included only to illustrate a possible secondary representation of the solved field not to compare FSC derived pathways to current state-of-the-art tractography methods.

3.5. FC LABEL PERMUTATION TEST

An unrestricted pair-label reassignment analysis was performed independently for each subject to determine how strongly the spatial placement of the functional constraints influenced the voxel-wise support maps. The selected 350 weights (50 from each network) retained their magnitudes and network grouping, while their anatomical endpoints were randomly permuted. In each permutation, 350 destination labels were sampled uniformly without replacement from all $\binom{200}{2} = 19900$ unordered Schaefer200 parcel pairs. Destination pairs could connect parcels anywhere in the brain. No network or anatomical stratification was imposed, and destination pairs were not matched to the observed pairs by distance or hemispheric class.

Whole-map resemblance was quantified for each network using the Pearson correlation between observed and permuted support values across graph nodes. Spatial correspondence of the strongest support was evaluated by selecting the highest-valued 5% of graph nodes in the observed and permuted maps and calculating their Dice overlap. Dice was calculated for the first 500 permutations. Distributions were summarized by the median, interquartile range, and 2.5th-97.5th percentiles. The across-network summary was the mean of the seven network-wise values within each permutation.

These reassignment distributions were treated as descriptive, subject-conditional sensitivity analyses rather than population-level hypothesis tests. Observed-map self-comparison equals one by definition and was therefore not treated as an independently estimated observed statistic, a rejection threshold, or a conventional permutation-test p value. The reported percentile intervals describe variation across seeded reassignments conditional on each subject's fixed structural graph and selected FC weights and not confidence intervals across subjects.

3.6. DESIKAN-KILLIANY COMPARISON WITH ORIGINAL FSC

To compare voxel-wise FSC directly with the previous region-level FSC framework,[24] the HCP analysis was repeated with the Desikan-Killiany parcellation restricted to 68 cortical regions.[38] This parcellation was used because it matched the original FSC study, allowing the voxel-wise formulation to be evaluated using the same regional definition and resting-state test-retest setting as the previous constrained-Laplacian analysis.

For each subject and resting-state run, Desikan-Killiany FC matrices were used as functional constraints on the subject- and voxel-wise FOD graph. In the original FSC framework, the constrained-Laplacian problem was solved on a regional tractography-derived structural connectome. Here, the same regional FC constraints were imposed on a voxel-wise FOD-derived conductance graph instead. This analysis therefore tested whether voxel-wise FSC preserved the behaviour of the original FSC framework when the regional parcellation was held fixed, while replacing the structural network with a voxel-wise diffusion-derived graph.

3.7. COMBINED TEST-RETEST ANALYSIS

Within-subject test-retest reproducibility was evaluated using both the Schaefer200 and Desikan-Killiany analyses across the four HCP resting-state runs: 1LR, 1RL, 2LR, and 2RL. Comparisons were restricted to matched phase-encoding directions: 1LR versus 2LR and 1RL versus 2RL in each of the three subjects, giving six comparisons per parcellation and method. Voxel-wise FSC was reduced to the corresponding parcellation scale by extracting one scalar response value for each imposed FC pair, producing a matching ROI-pair response vector. This reduction was used only for reproducibility analysis. The primary outputs remained the solved graph potentials, voxel-edge current fields, and support maps.

Reproducibility was quantified using Pearson correlation between complete ROI-pair vectors and the Jaccard index between the strongest 5% of ROI-pair values. In the Schaefer200 analysis, FC and voxel-wise FSC were evaluated at the finer parcellation scale. In the Desikan-Killiany analysis, FC, original region-level FSC, and voxel-wise FSC were evaluated in the same 68-region space, allowing direct comparison with the original FSC framework.[24] Results were summarized descriptively by the median and interquartile range across the six matched comparisons.

To examine whether the difference between Desikan-Killiany and Schaefer200 could reflect atlas construction rather than parcel number alone, the same test-retest analysis was repeated with the Schaefer 7-network atlas at 100, 200, 400, 600, 800, and 1,000 parcels. All three subjects and four resting-state runs were analysed, using the same

matched-direction comparisons, full-vector Pearson correlation, and top-5% Jaccard overlap.

4. RESULTS

4.1. IN-SILICO FIBERCUP SANITY CHECK

The in-silico FiberCup experiment showed that the voxel-wise FOD graph produced spatially plausible support patterns for the imposed functional relationships (Figure 3). The four relationships that were direct in the original tractography-derived FiberCup graph produced support along the expected fibre structures. The spatially isolated fourth relationship provided a specificity check: its support remained confined to the corresponding isolated bundle, indicating that the voxel-wise solution did not spread through unrelated parts of the phantom.

The fifth relationship illustrates an important difference between the previous region-level simulation and the present voxel-wise formulation. In the original FSC FiberCup experiment, this relationship was treated as indirect because the corresponding regions were not connected by a single edge in the tractography-derived regional structural graph.[24] In the voxel-wise FOD graph, however, the same relationship was supported through a shorter route enabled by the local crossing-FOD architecture visible in the phantom. This was not interpreted as a failure of the voxel-wise method. Instead, it shows that the structural possibilities available to voxel-wise FSC are defined by local FOD-supported voxel interfaces, not by the direct edges of the earlier region-level tractography graph.

This result highlights a limitation of using a region-level FiberCup graph as the reference for a voxel-wise FOD-graph method. A connection that is indirect in a region-level tractography graph may be locally feasible in the underlying FOD field. However, such a shortcut can have two different interpretations: it may reflect a genuine local crossing configuration that provides structural support at the voxel scale, or it may arise because the spatial or angular resolution of the phantom data is insufficient to separate nearby fibre structures. The latter is likely relevant in the FiberCup example, where the voxel-wise graph can exploit local FOD support that is not represented as a direct connection in the labelled region-level graph.

4.2. LOCAL GRAPH CONSTRUCTION FOLLOWED FOD GEOMETRY

Figure 4 illustrates how the local voxel-wise graph weights followed the FOD field. In the frontal corpus callosum example, where the FODs showed a coherent dominant orientation, the strongest voxel-voxel interface weights aligned with the principal fibre direction. Interfaces not supported by the dominant orientation had weaker endpoint support and lower combined weights. In the crossing-fibre example, high-weight interfaces followed multiple FOD-supported orientations rather than a single direction. These examples show that the voxel-wise structural graph was not defined by spatial adjacency alone, but by bidirectional FOD support at neighbouring voxel interfaces.

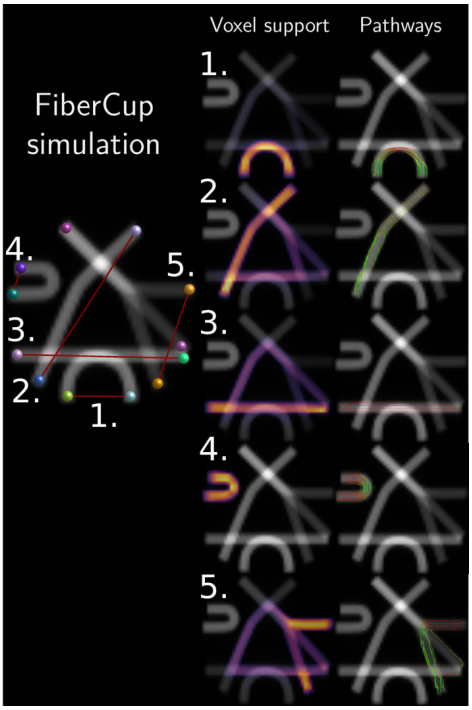

Figure 3. FiberCup simulation of voxel-wise FSC support and path-like summaries for five imposed functional relationships. The left panel shows the simulation setup, with coloured spheres denoting the functional nodes and red lines indicating the imposed functional constraints. The middle column shows normalized voxel-wise support maps, scaled independently from 0 to 1 for each relationship. The right column shows path-like summaries generated from the same voxel-wise current fields. Relationships 1-4 follow the expected FiberCup fibre structures, whereas relationship 5 follows a shorter route enabled by the local crossing-FOD architecture. The path-like curves are visualization summaries of the solved graph-flow field and should not be interpreted as conventional diffusion MRI tractography.

4.3. SCHAEFER200 NETWORK VISUALIZATIONS

Seven network-level maps were generated separately for all three subjects from Schaefer200 parcels grouped by their Yeo network labels. Figure 5 shows subject 419239 as the detailed example. Subtracting the L1-normalized unrestricted-null reference from each observed network map produced the residual maps shown in Figure 6. These highlight regions with greater or lower relative support compared with the shared null backbone, demonstrating FC-dependent spatial variation. The corresponding figures for subjects 130013 and 106824 are provided in the supplementary material. The maps contained a prominent shared deep-white-matter backbone. Visual and limbic support showed the clearest qualitative departures from the other networks, whereas control, default mode, dorsal attention, salience/ventral attention, and somatomotor support over-

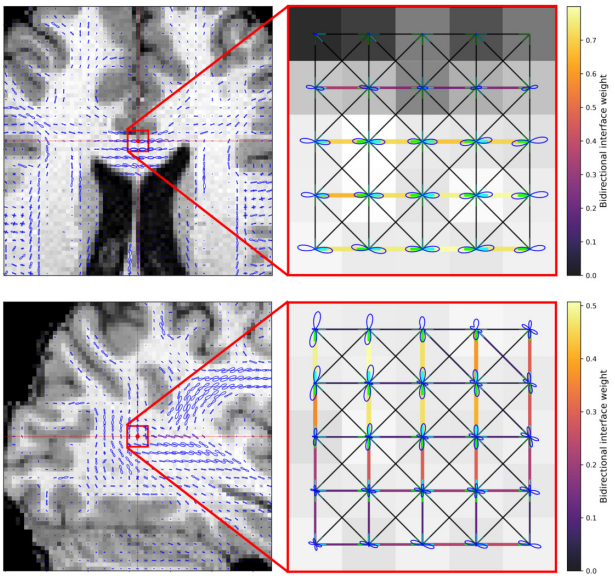

Figure 4. Local construction of the voxel-wise FSC graph in single-orientation and crossing-fibre white matter. The first row shows an axial view from the frontal corpus callosum, where the local FOD structure is dominated by a coherent left-right fibre orientation. The second row shows a sagittal view from a region with crossing or more complex fibre architecture. In each row, the left panel provides anatomical context and the right panel magnifies the selected voxel patch. Edge colour and thickness indicate the bidirectional interface weight between neighbouring voxels, computed from directional FOD support at both endpoints. In the corpus callosum example, high interface weights follow the dominant coherent fibre direction. In the crossing-fibre example, interface weights adapt to the locally multi-orientation FOD structure.

lapped strongly in several central regions. Parts of the network-associated features occupied spatial regions that were consistent with the expected locations of the corresponding functional networks, but this should not be read as direct evidence of anatomical network specificity.

The unrestricted reassignment analysis quantified the combination of shared and FC-location-dependent support (Fig. 7). Across-network median whole-map Pearson resemblance was 0.630 (2.5th-97.5th percentiles: 0.597-0.662) for subject 130013, 0.595 (0.559-0.630) for subject 106824, and 0.578 (0.543-0.612) for subject 419239. Median Dice overlap of the strongest 5% of graph nodes was 0.328 (0.298-0.358), 0.287 (0.260-0.320), and 0.312 (0.280-0.346), respectively. Thus, the permuted maps retained moderate resemblance to the observed maps because every realization used the same FOD-derived conductance graph, but none approached identity. The results show that the structural graph contributes a shared backbone, while reassigning the FC pairs produces substantial redistribution of voxel-wise support. Because the unrestricted destination pairs were not matched to the observed pairs by distance or hemispheric class, some of this redistribution may reflect differences in pair length or interhemispheric composition rather than FC-pair placement alone.

The somatomotor network was used to compare the voxel-wise FSC support map, a current-guided path-like display derived from the same solved edge-current field, and a conventional tractogram selected using the same network masks (Fig. 8). The three panels represent related but different quantities: a voxel-wise projection of edge-current magnitudes, a secondary path-like visualization of the graph-flow solution, and an endpoint-selected iFOD2/ACT streamline representation. No quantitative accuracy or performance comparison was made between them as the aim was to demonstrate the possibility of such visualisation of FSC output not to compare it against gold-standard tractography methods.

4.4. COMBINED TEST-RETEST REPRODUCIBILITY

Test-retest reproducibility was evaluated using the six matched-direction comparisons defined in the Methods. In the Desikan-Killiany analysis (Fig. 9), median FC reproducibility was $r = 0.829$ (interquartile range, IQR: 0.801-0.853), with a top-5% Jaccard overlap of 0.578 (0.538-0.603). Original region-level FSC had $r = 0.989$ (0.985-0.991) and Jaccard overlap 0.846 (0.806-0.865). Voxel-wise FSC had $r = 0.742$ (0.731-0.758) and Jaccard overlap 0.500 (0.481-0.520). These values are descriptive summaries across three subjects rather than population estimates.

At Schaefer200 (Fig. 10), median FC reproducibility was $r = 0.794$ (IQR: 0.762-0.815) and Jaccard overlap was 0.480 (0.421-0.527). Median voxel-wise FSC reproducibility was $r = 0.646$ (0.621-0.678) and Jaccard overlap was 0.410 (0.396-0.447). The lower values relative to Desikan-Killiany motivated the within-atlas multiscale analysis rather than being attributed solely to a conceptual difference between the two atlases.

The Schaefer multiscale analysis showed a gradual reduction in reproducibility as parcel number increased, rather than an abrupt difference specific to Schaefer200 (Table 1). Importantly, voxel-wise FSC reproducibility closely tracked the corresponding FC reproducibility across all six parcellation scales. From Schaefer100 to Schaefer1000, median FC Pearson correlation decreased from 0.810 to 0.713, an absolute reduction of 0.097, while median voxel-wise FSC correlation decreased from 0.668 to 0.581, a similar sized reduction of 0.087. FC top-5% Jaccard overlap decreased by 0.081, from 0.492 to 0.411, while voxel-wise FSC overlap decreased by 0.073, from 0.434 to 0.361. Intermediate scales followed the same monotonic or near-monotonic trajectories. These closely corresponding trends indicate that the reduction in voxel-wise FSC reproducibility at finer parcellation scales largely mirrors the declining reproducibility of the FC constraints supplied to the model, rather than representing an abrupt instability introduced by FSC.

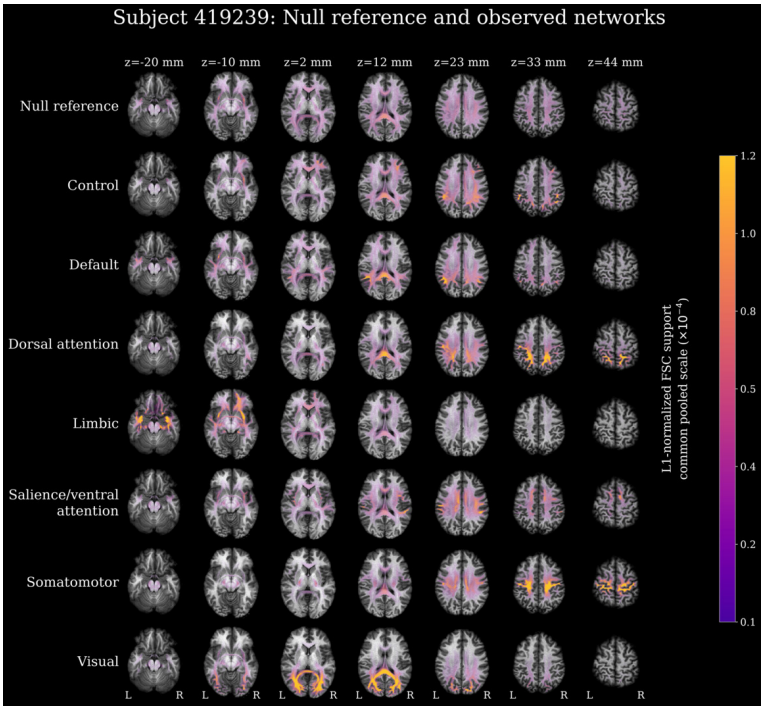

Figure 5. Null reference and observed voxel-wise FSC support maps for seven Schaefer200 networks in HCP subject 419239. The top row shows the expected support distribution under unrestricted FC-pair reassignment, and the remaining rows show the observed network maps. Each complete three-dimensional map was L1-normalized by its total positive support, and all rows use one common nonlinear pooled colour scale. The labelled z coordinates are in native diffusion space. Parts of the deep white matter are shared among networks, but each network shows a different spatial allocation of support relative to the null reference.

5. DISCUSSION

This work introduced voxel-wise function-structure coupling as a way to study how observed functional connectivity is accommodated by local diffusion-derived structure. Reducing dMRI to a regional tractography connectome can hide spatially extended or indirect contributions between functionally connected regions. Voxel-wise FSC instead constructs a subject-specific FOD-derived graph and imposes fMRI-derived FC values on that graph, producing potentials, edge-current fields, and support maps. These outputs are quantitative within the specified graph model, but they remain conditional on the functional constraints, diffusion model, graph-construction rules, and parcellation.

5.1. VOXEL-WISE FOD GRAPHS AS STRUCTURAL NETWORKS

The role of the voxel-wise FOD graph is illustrated at three complementary levels. The overall workflow in Figure 2 shows how regional FC constraints are connected to a subject- and voxel-wise structural network through ROI supernodes. The toy examples in Figure 1 illustrate the bidirectional endpoint rule used to assign conductance to voxel interfaces. The local HCP examples in Figure 4 then show how the same rule applies in real FOD fields, where coherent single-fibre regions and crossing-fibre regions produce different local graph geometries.

Together, these examples clarify that voxel-wise FSC does not treat the white-matter mask as a uniform conductive medium. The conductance field is locally anisotropic and depends on FOD-derived directional support, following the broader use of spherical deconvolution and FODs to represent complex fibre configurations beyond the single-tensor model.[9,28,46] This is important because many white-matter regions contain crossing, kissing, fanning, or otherwise complex fibre configurations that are not adequately represented by a single dominant tensor direction.[6,44] The bidirectional endpoint rule also makes the graph more conservative than a one-sided orientation rule: high conductance requires compatible FOD support on both sides of the voxel interface. This neighbourhood-aware interpretation is consistent with the observation that adjacent voxels contain information about local fibre geometry that is not captured by treating each voxel independently.[29]

This interpretation also defines an important limitation. The voxel-wise structural network can only be as reliable as the FOD estimates from which it is built. Local uncertainty, partial-volume effects, angular resolution, response-function estimation, preprocessing choices, and FOD modelling assumptions are known to influence diffusion MRI-derived structural representations.[7-9,46] Voxel-wise FSC should therefore be interpreted as FC-conditioned flow over a diffusion-derived graph, not as a direct measurement of axonal wiring or causal neural signaling.

Native voxel resolution does not necessarily imply that the resulting localization is accurate at the scale of an in-

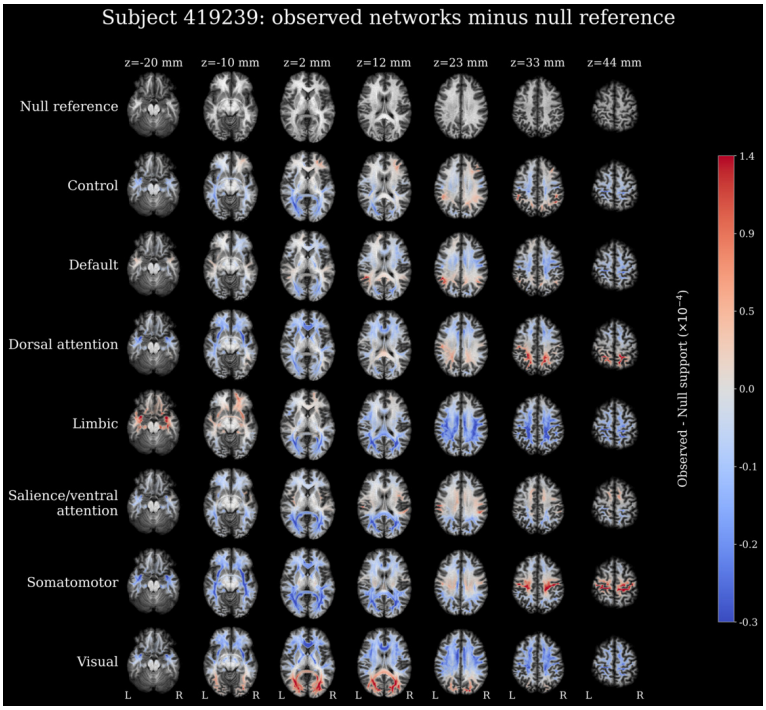

Figure 6. Residual support after subtracting the L1-normalized unrestricted-null reference from each L1-normalized observed network map in HCP subject 419239. The top row represents zero residual. Red indicates a larger fraction of total support than the null reference and blue indicates a smaller fraction. All rows use one common zero-centred diverging scale, with the negative and positive ranges scaled separately. Colour-bar values use the multiplier shown beside the scale. The labelled z coordinates are in native diffusion space. This illustrates that the null reference does not represent any of the networks completely.

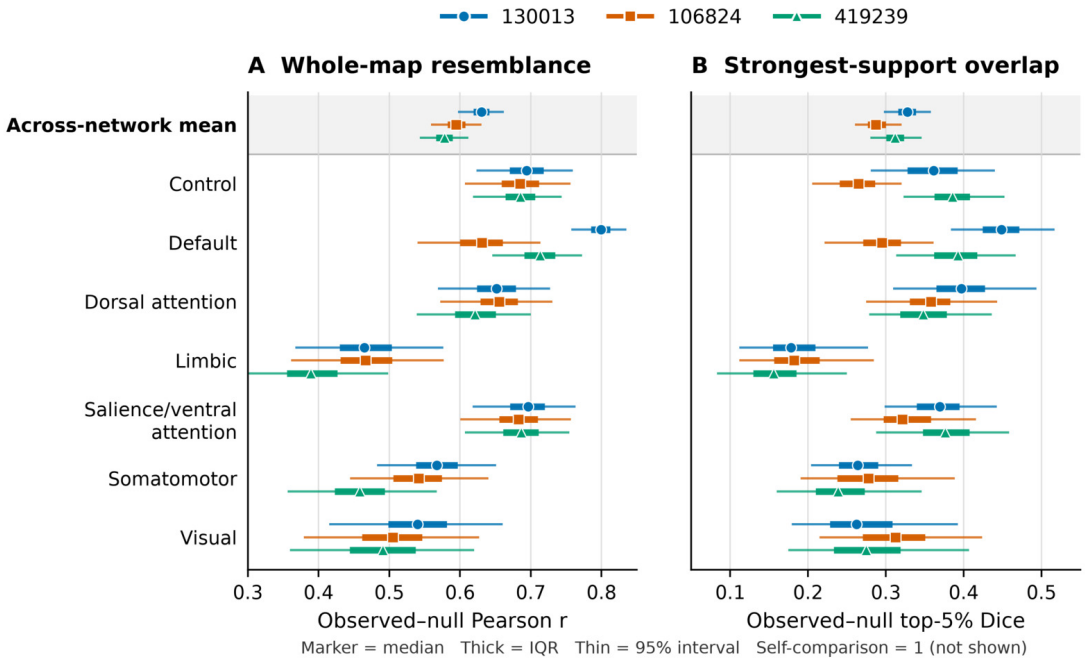

Figure 7. Unrestricted whole-cortex FC-pair reassignment across three HCP subjects. Panel **A** shows whole-map Pearson resemblance and Panel **B** top-5% Dice overlap. Markers denote medians, thick segments interquartile ranges, and thin segments 2.5th–97.5th percentiles. The distributions are descriptive and subject-conditional, not population confidence intervals. Moderate whole-map resemblance indicates shared influence of the structural conductance graph, whereas incomplete correspondence shows that constraint placement changes the FSC maps.

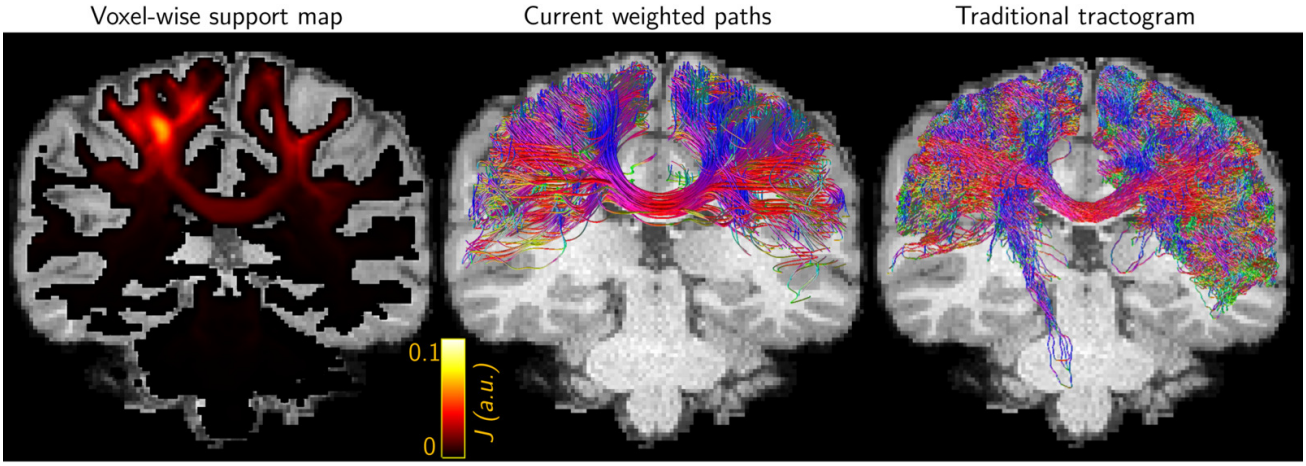

Figure 8. Voxel-wise FSC and conventional tractography representations of the somatomotor network in subject 419239. Left: voxel-wise FSC support obtained by imposing resting-state functional constraints between somatomotor parcels on the subject-specific FOD-derived graph. Middle: a current-guided path-like display derived from the same solved edge-current field. These curves summarize high-current components and are not conventional diffusion MRI streamlines. Right: a conventional tractogram selected with the same somatomotor masks. The panels illustrate differences between distributed FSC support, a graph-flow summary, and an endpoint-selected streamline representation but do not constitute a quantitative benchmark or evidence that one representation is anatomically more accurate.



Figure 9. Desikan-Killiany within-subject test-retest reproducibility across HCP resting-state runs. FC, original region-level FSC, and voxel-wise FSC were evaluated between the runs 1LR, 2LR, 1RL, and 2RL using ROI-pair response vectors. Original FSC showed the highest reproducibility, consistent with its dependence on the stable conventional SC matrix. Voxel-wise FSC showed lower but meaningful reproducibility, indicating that parcellation-level summaries derived from the voxel-wise FOD graph were stable across repeated fMRI runs.

dividual voxel. Registration errors, tissue partial volume, uncertainty in local FODs, and the mismatch between the spatial point-spread characteristics of fMRI and the diffusion grid can all perturb the graph interfaces and imposed boundary conditions. Coarser parcellations partly average these effects, whereas a voxel-wise output exposes them. The maps should therefore be interpreted as high-resolution model fields whose effective biological resolution may be coarser than the displayed grid.

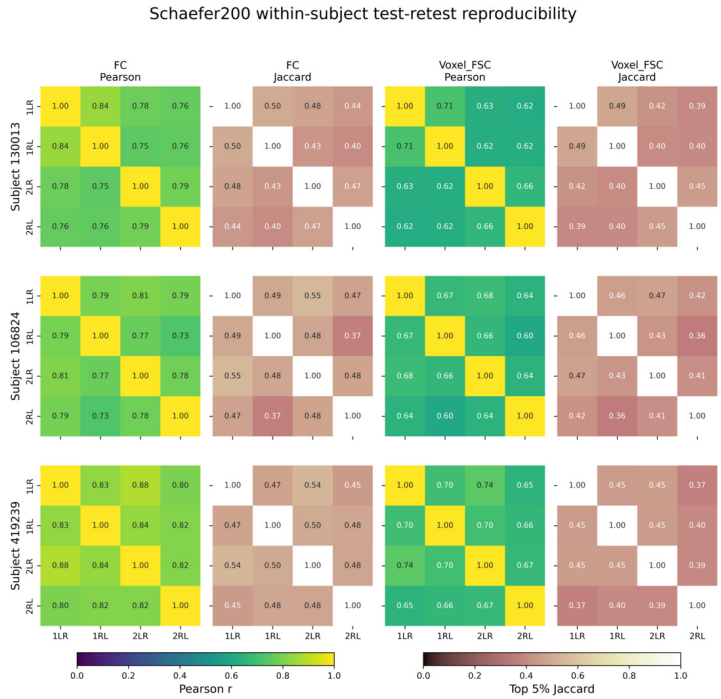

Figure 10. Schaefer200 test-retest reproducibility of FC and voxel-wise FSC across HCP resting-state runs. Reproducibility was evaluated between the runs 1LR, 2LR, 1RL, and 2RL using Pearson correlation and top-5% Jaccard overlap. Voxel-wise FSC retained meaningful test-retest stability at the finer parcellation scale.

Table 1. Within-subject reproducibility across Schaefer parcellation scales. Values are median [interquartile range] across six observations: three subjects and two matched phase-encoding comparisons per subject (REST1_LR–REST2_LR and REST1_RL– REST2_RL).

Scale	FC Pearson r	Voxel-FSC Pearson r	FC top-5% Jaccard	Voxel-FSC top-5% Jaccard
Schaefer100	0.810 [0.798–0.831]	0.668 [0.655–0.691]	0.492 [0.457–0.547]	0.434 [0.414–0.483]
Schaefer200	0.794 [0.762–0.815]	0.646 [0.621–0.678]	0.480 [0.421–0.527]	0.410 [0.396–0.447]
Schaefer400	0.766 [0.728–0.790]	0.618 [0.601–0.660]	0.436 [0.410–0.472]	0.393 [0.362–0.435]
Schaefer600	0.744 [0.706–0.769]	0.605 [0.591–0.645]	0.422 [0.402–0.459]	0.383 [0.345–0.415]
Schaefer800	0.723 [0.682–0.754]	0.590 [0.577–0.633]	0.412 [0.395–0.452]	0.367 [0.344–0.398]
Schaefer1000	0.713 [0.670–0.744]	0.581 [0.565–0.623]	0.411 [0.385–0.447]	0.361 [0.335–0.393]

5.2. NETWORK-LEVEL SUPPORT AND PARCELLATION SCALE

Schaefer200 provides a multi-resolution cortical parcellation derived from functional connectivity, and its parcels can be grouped by canonical Yeo functional-network assignments.[37,49] Smaller parcels provide more localized interfaces between FC constraints and the FOD graph, while the network assignments provide a defined way to aggregate pairwise solutions. In all three subjects, some network-associated features occupied spatial regions that were consistent with the expected locations of the corresponding functional networks. The detailed example in Figure 5 also shows overlap among several networks in deep white matter which is expected as many white matter bundles traverse via same regions. The maps therefore demonstrate that the method produces spatially resolved, FC-conditioned fields, but they do not by themselves demonstrate anatomical network specificity.

The permutation test helps distinguish two contributions to this pattern. Moderate observed-null correlations and Dice overlaps show that the fixed conductance graph produces a shared structural backbone, whereas the substantial departure from identity shows that changing the locations of the FC constraints redistributes support. This does not reject either shared white-matter architecture or conductance dominance. Both can coexist with FC-configuration-dependent variation. The analysis therefore indicates that network-associated support maps depend on FC-pair assignment, although the unrestricted design does not separate general placement effects from differences in pair length or hemispheric composition. Anatomical network specificity needs further validation.

The result also depends on the selected within-network FC pairs, parcellation, ROI interfaces, and subject-specific

FOD graph. This caution is consistent with previous work showing that parcellation choice and scale affect functional-connectivity estimates, graph measures, and connectome interpretation.[50,51] The comparison between Figure 9 and Figure 10 initially suggested lower reproducibility at the finer atlas, and the Schaefer100-1000 analysis confirmed a gradual decline within a single atlas family. Test-retest reliability is known to vary with node definition and other methodological choices.[52,53] The multiscale results therefore identify parcel resolution as one contributor, without excluding differences in atlas construction or ROI-interface geometry.

5.3. TASK ACTIVATION AND PAIRWISE FUNCTIONAL CONSTRAINTS

An important limitation concerns task-fMRI activation within the present FSC formulation. A task general linear model contrast quantifies the response of individual regions to an experimental condition, whereas functional connectivity describes statistical dependence between pairs of regional time series. Regions can respond consistently to the same task without exhibiting correspondingly strong pairwise coupling. This distinction is longstanding.[54-56] It also motivates separating task-evoked responses from residual or background connectivity when estimating task-related coupling.[57,58]

The present FSC formulation is most directly applied to pairwise inputs or to a grounded network which can be built readily from resting-state correlations. A task-fMRI extension would require additional choices about task-responsive regions, removal of evoked responses, estimation of task-dependent connectivity, and translation of node-wise activation into pairwise potential constraints. Treating activation as an externally driven nodal source would instead require a different source model and independent validation. Such an extension is methodologically substantial and outside the scope of this study.

5.4. CONTINUITY WITH THE ORIGINAL FSC FRAMEWORK

The Desikan-Killiany analysis evaluated voxel-wise FSC in the same regional setting as the original constrained-Laplacian FSC framework.[24] This comparison is shown in Figure 9. Original FSC showed very high test-retest reproducibility, consistent with its use of a stable regional tractography-derived SC matrix. Voxel-wise FSC showed lower but still meaningful reproducibility, reflecting the central methodological change of the present work: the structural network is no longer a regional SC matrix, but a subject-wise FOD-derived voxel graph whose local conductances are defined on voxel interfaces (Figures 2 and 4).

This preserves the constrained-Laplacian logic of the original FSC framework while changing the spatial scale at which structural support is modelled. The result is consistent with previous function-structure coupling works showing that functional connectivity is shaped by structural architecture but is not a one-to-one readout of direct anatomical connections.[11,12,15,59] The parcellation-level ROI-pair response vectors used in Figure 9 should therefore be interpreted as reduced summaries for reproducibility analysis. The primary outputs of voxel-wise FSC remain the spatially resolved graph potentials, voxel-edge current fields, and support maps, as illustrated by the somatomotor example in Figure 8.

5.5. RELATIONSHIP TO TRACTOGRAPHY AND PATH-LIKE DISPLAYS

Voxel-wise FSC is related to graph-theoretical tractography only in the sense that dMRI is used to define a local voxel graph. Earlier graph-based and optimization-based tractography methods used diffusion information to search for likely anatomical paths through such graphs.[17,18,21,23,25,26] Voxel-wise FSC uses a different operation: the graph is not searched for the most likely anatomical pathway, but is used as the structural network on which observed functional constraints are solved (Figures 2 and 4). However, this does not make FSC free of error sources related to FOD estimates and tractography.[7-9,46]

In voxel-wise FSC, the primary output is not a reconstructed tractogram, but the solved voxel-wise support field. Path-like displays can still be useful because they summarize high-current components of the graph-flow solution in a familiar streamline form, as shown in the Fiber-Cup and somatomotor examples (Figures 3 and 8). However, these curves are downstream visualizations of the solved current field and should not be interpreted as edge-currents imposed onto conventional diffusion MRI tractography.

The somatomotor comparison in Figure 8 is consequently illustrative rather than a performance benchmark against state-of-the-art tractography methods. The conventional tractogram provides an endpoint-selected anatomical reference for the same cortical masks, whereas voxel-wise FSC shows where the observed somatomotor FC constraints load onto the FOD-derived graph. The two representations may overlap where strong functional constraints follow major diffusion-consistent pathways, but they need not be identical because they answer different questions: tractography asks which anatomical streamlines are reconstructed from the diffusion data, whereas voxel-wise FSC asks how observed functional relationships are accommodated by the diffusion-derived structural network.

5.6. LIMITATIONS AND FUTURE WORK

The present analyses were methodological demonstrations rather than population-level validation. The HCP evaluation included only three subjects. Seven-network support maps were generated separately for all three subjects. The subject 419239 is presented as the detailed main-text example (Figure 5) and the corresponding maps for subjects 130013 and 106824 are provided in the supplementary material. Because the sample comprised only three subjects, no population-level statistical inference was attempted. The reported statistics and subject-conditional reassignment distributions are descriptive. Larger datasets would be needed to evaluate group-level reproducibility, inter-subject variability, stability across preprocessing choices, and

feasibility for investigating different brain conditions and diseases. The FiberCup experiment provided an implementation-level sanity check for graph construction, constraint encoding, and pairwise support extraction (Figure 3), but it was not a definitive ground truth for voxel-wise anatomical routing. A connection that is indirect in a region-level tractography graph may be locally feasible in a voxel-wise FOD graph, either because such local support exists or because the spatial or angular resolution is insufficient to separate nearby fibre structures. Voxel-wise FSC streamlines should be regarded as a proof-of-concept, not an anatomically validated replacement for tractography. The anatomical validation of voxel-wise FSC remains substantially more limited than the extensive external benchmarking available for tractography.

6. CONCLUSION

This work proposed voxel-wise function-structure coupling as a quantitative framework for studying how observed functional connectivity is supported by local diffusion-derived structural architecture. The method constructs a subject-wise FOD-derived voxel graph, imposes observed fMRI-derived functional connectivity values on that graph, and solves for spatially resolved support maps. This allows functional relationships to be studied in relation to distributed, indirect, and crossing-fibre structural support that may be poorly represented by single parcel-to-parcel edges. The method was evaluated using in-silico simulations, local graph-construction examples, multiple brain parcellations, network-level visualisations, and within-subject test-retest analyses. Together, these results show that voxel-wise FSC provides a reproducible and spatially resolved way to map functional relationships onto diffusion-derived structural support, with possibility to produce tractogram-like visualizations for qualitative analyses.

ETHICS STATEMENT

This study used previously collected, publicly available, and de-identified Human Connectome Project data. No new human participant data were collected for this work. The HCP data collection was conducted under the ethical approvals and informed-consent procedures of the original HCP study. The in-silico phantom analyses did not involve human participants or animal subjects.

DATA AND CODE AVAILABILITY

The voxel-wise FSC code is openly available at https://github.com/vilsaira/fscpy. The Human Connectome Project data used in this study are available through the HCP data repository under the applicable data-use terms. The FiberCup phantom data are available from the original FiberCup resource described in the cited publications.

AUTHOR CONTRIBUTIONS

Viljami Sairanen: Conceptualization, Methodology, Software, Formal analysis, Investigation, Visualization, Writing.

FUNDING

N/A

DECLARATION OF COMPETING INTERESTS

The author declares no competing interests.

USE OF AI

AI tools were used for language editing, code editing, and drafting support during manuscript preparation; all scientific content, analyses, interpretation, and final text were reviewed and approved by the author.

ACKNOWLEDGEMENTS

The author thanks the anonymous reviewers for their motivating and thoughtful feedback. In particular, their suggestions to perform permutation-based analyses and evaluate multiple Schaefer parcellation scales strengthened the methodological evaluation and helped clarify the interpretation and limitations of the proposed framework.

The author is also grateful to an unnamed mentor for encouraging in pursuing independent research ideas.

The authors wish to thank the Finnish Computing Competence Infrastructure (FCCI) for supporting this project with computational and data storage resources. Open access funded by Helsinki University Library.

Submitted: July 11, 2026 CDT. Revised: September 04, 2026 CDT; September 25, 2026 CDT. Accepted: October 05, 2026 CDT. Published: October 19, 2026 CDT.

This is an open-access article distributed under the terms of the Creative Commons Attribution 4.0 International License (CCBY-4.0). View this license's legal deed at http://creativecommons.org/licenses/by/4.0 and legal code at http://creativecommons.org/licenses/by/4.0/legalcode for more information.

REFERENCES

1. Friston KJ. Functional and effective connectivity: A review. *Brain Connectivity*. 2011;1(1):13-36. doi:10.1089/brain.2011.0008

2. Fox MD, Snyder AZ, Vincent JL, Corbetta M, Van Essen DC, Raichle ME. The human brain is intrinsically organized into dynamic, anticorrelated functional networks. *Proceedings of the National Academy of Sciences*. 2005;102(27):9673-9678. doi:10.1073/pnas.0504136102

3. Raichle ME, MacLeod AM, Snyder AZ, Powers WJ, Gusnard DA, Shulman GL. A default mode of brain function. *Proceedings of the national academy of sciences*. 2001;98(2):676-682.

4. Basser PJ, Mattiello J, LeBihan D. MR diffusion tensor spectroscopy and imaging. *Biophysical Journal*. 1994;66(1):259-267. doi:10.1016/S0006-3495(94)80775-1

5. Le Bihan D, Mangin JF, Poupon C, et al. Diffusion tensor imaging: Concepts and applications. *Journal of Magnetic Resonance Imaging*. 2001;13(4):534-546. doi:10.1002/jmri.1076

6. Johansen-Berg H, Rushworth MFS. Using diffusion imaging to study human connectional anatomy. *Annual Review of Neuroscience*. 2009;32(1):75-94. doi:10.1146/annurev.neuro.051508.135735

7. Maier-Hein KH, Neher PF, Houde JC, et al. The challenge of mapping the human connectome based on diffusion tractography. *Nature Communications*. 2017;8(1):1-13. doi:10.1038/s41467-017-01285-x

8. Schilling KG, Daducci A, Maier-Hein K, et al. Challenges in diffusion MRI tractography – lessons learned from international benchmark competitions. *Magnetic Resonance Imaging*. 2019;57:194-209. doi:10.1016/j.mri.2018.11.014

9. Jeurissen B, Descoteaux M, Mori S, Leemans A. Diffusion MRI fiber tractography of the brain. *NMR in Biomedicine*. 2019;32(4):e3785. doi:10.1002/nbm.3785

10. Sotiropoulos SN, Zalesky A. Building connectomes using diffusion MRI: Why, how and but. *NMR in Biomedicine*. 2019;32(4):e3752. doi:10.1002/nbm.3752

11. Honey CJ, Sporns O, Cammoun L, et al. Predicting human resting-state functional connectivity from structural connectivity. *Proceedings of the National Academy of Sciences*. 2009;106(6):2035-2040. doi:10.1073/pnas.0811168106

12. Abdelnour F, Voss HU, Raj A. Network diffusion accurately models the relationship between structural and functional brain connectivity networks. *NeuroImage*. 2014;90:335-347. doi:10.1016/j.neuroimage.2013.12.039

13. Avena-Koenigsberger A, Misic B, Sporns O. Communication dynamics in complex brain networks. *Nature Reviews Neuroscience*. 2018;19(1):17-33. doi:10.1038/nrn.2017.149

14. Seguin C, Tian Y, Zalesky A. Network communication models improve the behavioral and functional predictive utility of the human structural connectome. *Network Neuroscience*. 2020;4(4):980-1006. doi:10.1162/netn_a_00161

15. Suárez LE, Markello RD, Betzel RF, Misic B. Linking structure and function in macroscale brain networks. *Trends in Cognitive Sciences*. 2020;24(4):302-315. doi:10.1016/j.tics.2020.01.008

16. Fotiadis P, Parkes L, Davis KA, Satterthwaite TD, Shinohara RT, Bassett DS. Structure–function coupling in macroscale human brain networks. *Nature Reviews Neuroscience*. 2024;25(10):688-704. doi:10.1038/s41583-024-00846-6

17. Iturria-Medina Y, Canales-Rodríguez EJ, Melie-García L, et al. Characterizing brain anatomical connections using diffusion weighted MRI and graph theory. *NeuroImage*. 2007;36(3):645-660. doi:10.1016/j.neuroimage.2007.02.012

18. Iturria-Medina Y, Sotero RC, Canales-Rodríguez EJ, Alemán-Gómez Y, Melie-García L. Studying the human brain anatomical network via diffusion-weighted MRI and graph theory. *NeuroImage*. 2008;40(3):1064-1076. doi:10.1016/j.neuroimage.2007.10.060

19. Parker GJM, Stephan KE, Barker GJ, et al. Initial demonstration of in vivo tracing of axonal projections in the macaque brain and comparison with the human brain using diffusion tensor imaging and fast marching tractography. *NeuroImage*. 2002;15(4):797-809. doi:10.1006/nimg.2001.0994

20. Jbabdi S, Bellec P, Toro R, Daunizeau J, Pélégrini-Issac M, Benali H. Accurate anisotropic fast marching for diffusion-based geodesic tractography. *International Journal of Biomedical Imaging*. 2008;2008(1):320195. doi:10.1155/2008/320195

21. Jbabdi S, Woolrich MW, Andersson JLR, Behrens TEJ. A bayesian framework for global tractography. *NeuroImage*. 2007;37(1):116-129. doi:10.1016/j.neuroimage.2007.04.039

22. Descoteaux M, Deriche R, Knosche TR, Anwander A. Deterministic and probabilistic tractography based on complex fibre orientation distributions. *IEEE Transactions on Medical Imaging*. 2009;28(2):269-286. doi:10.1109/TMI.2008.2004424

23. Reisert M, Mader I, Anastasopoulos C, Weigel M, Schnell S, Kiselev V. Global fiber reconstruction becomes practical. *NeuroImage*. 2011;54(2):955-962. doi:10.1016/j.neuroimage.2010.09.016

24. Sairanen V. From nodes to pathways: An edge-centric model of brain function–structure coupling via constrained laplacians. *Network Neuroscience*. Published online May 2026:1-21. doi:10.1162/NETN.a.589

25. Sotiropoulos SN, Bai L, Morgan PS, Constantinescu CS, Tench CR. Brain tractography using q-ball imaging and graph theory: Improved connectivities through fibre crossings via a model-based approach. *NeuroImage*. 2010;49(3):2444-2456. doi:10.1016/j.neuroimage.2009.10.001

26. Cieslak M, Brennan T, Meiring W, et al. Analytic tractography: A closed-form solution for estimating local white matter connectivity with diffusion MRI. *NeuroImage*. 2018;169:473-484. doi:10.1016/j.neuroimage.2017.12.039

27. Behjat H, Tarun A, Abramian D, Larsson M, Ville DVD. Voxel-wise brain graphs from diffusion MRI: Intrinsic eigenspace dimensionality and application to functional MRI. *IEEE Open Journal of Engineering in Medicine and Biology*. 2025;6:158-167. doi:10.1109/OJEMB.2023.3267726

28. Tournier JD, Calamante F, Connelly A. Robust determination of the fibre orientation distribution in diffusion MRI: Non-negativity constrained super-resolved spherical deconvolution. *NeuroImage*. 2007;35(4):1459-1472. doi:10.1016/j.neuroimage.2007.02.016

29. Bastiani M, Cottaar M, Dikranian K, et al. Improved tractography using asymmetric fibre orientation distributions. *NeuroImage*. 2017;158:205-218. doi:10.1016/j.neuroimage.2017.06.050

30. Chung FRK. *Spectral Graph Theory*. Vol 92. American Mathematical Society; 1997.

31. Shuman DI, Narang SK, Frossard P, Ortega A, Vandergheynst P. The emerging field of signal processing on graphs: Extending high-dimensional data analysis to networks and other irregular domains. *IEEE signal processing magazine*. 2013;30(3):83-98.

32. Chung-Wen Ho, Ruehli A, Brennan P. The modified nodal approach to network analysis. *IEEE Transactions on Circuits and Systems*. 1975;22(6):504-509. doi:10.1109/TCS.1975.1084079

33. Wedepohl LM, Jackson L. Modified nodal analysis: An essential addition to electrical circuit theory and analysis. *Engineering Science & Education Journal*. 2002;11(3):84-92. doi:10.1049/esej:20020301

34. Atasoy S, Donnelly I, Pearson J. Human brain networks function in connectome-specific harmonic waves. *Nature Communications*. 2016;7(1):10340. doi:10.1038/ncomms10340

35. Abdelnour F, Dayan M, Devinsky O, Thesen T, Raj A. Functional brain connectivity is predictable from anatomic network's laplacian eigen-structure. *NeuroImage*. 2018;172:728-739. doi:10.1016/j.neuroimage.2018.02.016

36. Smith RE, Tournier JD, Calamante F, Connelly A. SIFT2: Enabling dense quantitative assessment of brain white matter connectivity using streamlines tractography. *NeuroImage*. 2015;119:338-351. doi:10.1016/j.neuroimage.2015.06.092

37. Schaefer A, Kong R, Gordon EM, et al. Local-global parcellation of the human cerebral cortex from intrinsic functional connectivity MRI. *Cerebral Cortex*. 2018;28(9):3095-3114. doi:10.1093/cercor/bhx179

38. Desikan RS, Ségonne F, Fischl B, et al. An automated labeling system for subdividing the human cerebral cortex on MRI scans into gyral based regions of interest. *NeuroImage*. 2006;31(3):968-980. doi:10.1016/j.neuroimage.2006.01.021

39. Poupon C, Rieul B, Kezele I, Perrin M, Poupon F, Mangin JF. New diffusion phantoms dedicated to the study and validation of high-angular-resolution diffusion imaging (HARDI) models. *Magnetic Resonance in Medicine: An Official Journal of the International Society for Magnetic Resonance in Medicine*. 2008;60(6):1276-1283.

40. Poupon C, Laribiere L, Tournier G, et al. A diffusion hardware phantom looking like a coronal brain slice. In: *Proceedings of the International Society for Magnetic Resonance in Medicine*. Vol 18. ; 2010:581.

41. Fillard P, Descoteaux M, Goh A, et al. Quantitative evaluation of 10 tractography algorithms on a realistic diffusion MR phantom. *Neuroimage*. 2011;56(1):220-234.

42. Van Essen DC, Smith SM, Barch DM, Behrens TEJ, Yacoub E, Ugurbil K. The WU-minn human connectome project: An overview. *NeuroImage*. 2013;80:62-79. doi:10.1016/j.neuroimage.2013.05.041

43. Glasser MF, Sotiropoulos SN, Wilson JA, et al. The minimal preprocessing pipelines for the human connectome project. *NeuroImage*. 2013;80:105-124. doi:10.1016/j.neuroimage.2013.04.127

44. Sotiropoulos SN, Jbabdi S, Xu J, et al. Advances in diffusion MRI acquisition and processing in the human connectome project. *NeuroImage*. 2013;80:125-143. doi:10.1016/j.neuroimage.2013.05.057

45. Dhollander T, Raffelt D, Connelly A. Unsupervised 3-tissue response function estimation from single-shell or multi-shell diffusion MR data without a co-registered T1 image. In: *ISMRM Workshop on Breaking the Barriers of Diffusion MRI*. Vol 5. Lisbon; 2016.

46. Tournier JD, Smith R, Raffelt D, et al. MRtrix3: A fast, flexible and open software framework for medical image processing and visualisation. *NeuroImage*. 2019;202:116137. doi:10.1016/j.neuroimage.2019.116137

47. Smith RE, Tournier JD, Calamante F, Connelly A. Anatomically-constrained tractography: Improved diffusion MRI streamlines tractography through effective use of anatomical information. *NeuroImage*. 2012;62(3):1924-1938. doi:10.1016/j.neuroimage.2012.06.005

48. Sairanen V, Ocampo-Pineda M, Granziera C, Schiavi S, Daducci A. Incorporating outlier information into diffusion-weighted MRI modeling for robust microstructural imaging and structural brain connectivity analyses. *Neuroimage*. 2022;247:118802.

49. Yeo BT, Krienen FM, Sepulcre J, et al. The organization of the human cerebral cortex estimated by intrinsic functional connectivity. *Journal of Neurophysiology*. 2011;106(3):1125-1165. doi:10.1152/jn.00338.2011

50. Zalesky A, Fornito A, Bullmore ET. Network-based statistic: Identifying differences in brain networks. *Neuroimage*. 2010;53(4):1197-1207.

51. Bryce NV, Flournoy JC, Moreira JFG, et al. Brain parcellation selection: An overlooked decision point with meaningful effects on individual differences in resting-state functional connectivity. *NeuroImage*. 2021;243:118487.

52. Termenon M, Jaillard A, Delon-Martin C, Achard S. Reliability of graph analysis of resting state fMRI using test-retest dataset from the human connectome project. *Neuroimage*. 2016;142:172-187.

53. Noble S, Scheinost D, Constable RT. A decade of test-retest reliability of functional connectivity: A systematic review and meta-analysis. *Neuroimage*. 2019;203:116157.

54. Friston KJ. Functional and effective connectivity in neuroimaging: A synthesis. *Human Brain Mapping*. 1994;2(1–2):56-78. doi:10.1002/hbm.460020107

55. Friston KJ, Buechel C, Fink GR, Morris J, Rolls E, Dolan RJ. Psychophysiological and modulatory interactions in neuroimaging. *NeuroImage*. 1997;6(3):218-229. doi:10.1006/nimg.1997.0291

56. Rissman J, Gazzaley A, D'Esposito M. Measuring functional connectivity during distinct stages of a cognitive task. *NeuroImage*. 2004;23(2):752-763. doi:10.1016/j.neuroimage.2004.06.035

57. Fair DA, Schlaggar BL, Cohen AL, et al. A method for using blocked and event-related fMRI data to study "resting state" functional connectivity. *NeuroImage*. 2007;35(1):396-405. doi:10.1016/j.neuroimage.2006.11.051

58. Cole MW, Ito T, Schultz D, Mill R, Chen R, Cocuzza C. Task activations produce spurious but systematic inflation of task functional connectivity estimates. *NeuroImage*. 2019;189:1-18. doi:10.1016/j.neuroimage.2018.12.054

59. Messé A, Rudrauf D, Giron A, Marrelec G. Predicting functional connectivity from structural connectivity via computational models using MRI: An extensive comparison study. *NeuroImage*. 2015;111:65-75. doi:10.1016/j.neuroimage.2015.02.001

SUPPLEMENTARY MATERIALS

FUNGUS_supplement.pdf

Download: https://apertureneuro.org/article/172225-voxel-wise-function-structure-coupling-with-diffusion-weighted-and-functional-mri/attachment/370259.pdf